



Cite this: DOI: 10.1039/c8ce00057c

Controlled preparation of high quality WS₂ nanostructures by a microwave-assisted solvothermal method†

 Haiting Yan,^a Jianhui Li,^a Daomeng Liu,^a Xunan Jing,^a
Daquan Wang^a and Lingjie Meng^{id} *^{ab}

Thin-layered WS₂ nanostructures have attracted great attention owing to their superior structures and properties when compared to MoS₂, including larger layer-spacing, higher energy gap and better photo-thermal and lubrication properties. However, it is still challenging to prepare high-quality WS₂ nanosheets and assemble them into large quantities. In this work, we report a facile and efficient microwave-assisted solvothermal method for the synthesis of WS₂ nanostructures in *N*-methyl-2-pyrrolidone (NMP) using cheap tungsten hexachloride (WCl₆) and elemental sulfur (S) as starting materials. The formation of WS₂ nanosheets and their controlled assembly into different morphologies (such as nanocones and nanoworms) were studied by adjusting the reactant concentration and reaction temperature. This method has also been successfully applied for preparation of other transition-metal dichalcogenides such as MoS₂. The resulting WS₂ and MoS₂ nanomaterials were characterized by transmission electron microscopy (TEM), scanning electron microscopy (SEM), X-ray diffraction (XRD), X-ray photoelectron spectroscopy (XPS) and Raman spectroscopy. The photothermal properties of WS₂ nanostructures have been investigated and it was found that the WS₂ nanosheets have the best photothermal efficiency and stable photothermal capacity, exhibiting great potential for photothermal therapy and other fields.

 Received 14th January 2018,
Accepted 14th March 2018

DOI: 10.1039/c8ce00057c

rsc.li/crystengcomm

Introduction

Thin-layered transition metal dichalcogenides (TMDs), including MoS₂, WS₂, MoSe₂, WSe₂, and their derivatives, are becoming very popular because of their two-dimensional structures and unique electronic, optical and chemical properties.^{1–3} Similar to graphene, TMDs have layered structures and the interlayers of TMDs are stacked together by van der Waals forces. Each TMD monolayer consists of three atomic layers, in which a transition metal layer is sandwiched between two chalcogen layers.⁴ Unlike graphene, most of these TMDs are semiconductors in nature and possess larger interlayer spacing, exhibiting superior application potential in lithium ion batteries,^{5,6} field effect transistors,^{7,8} hydrogen evolution catalysis,^{9–11} biomedical applications,^{12,13} and many others. The quality of TMDs and the related properties and

applications rely largely on their preparation method. Therefore, mass preparation of high-quality TMDs with tunable structures and morphologies is a key issue that needs to be addressed.

A wide variety of synthetic methods have been developed for the preparation of thin-layered TMDs. In general, these methods can be divided into two basic categories: top-down approaches, which include mechanical cleavage and liquid exfoliation, and bottom-up approaches, such as chemical vapor deposition (CVD) growth and wet chemical synthesis.^{2,14} Top-down methods have been widely used to produce high-quality TMD sheets through exfoliation of various high purity and layered TMD crystals.^{15–17} However, the low yield and slow production rate of the top-down methods make them difficult to meet the demands in various practical applications. Compared to top-down methods, bottom-up approaches are more versatile because a variety of different precursors can be used. The CVD technique has the highest level of control among all other synthetic methods for ultrathin TMDs and other 2D nanomaterials because it allows scalable batch size and controllable thickness. And remarkably, the crystal quality, purity and properties of TMD nanosheets obtained from CVD methods are comparable to those of exfoliated thin layers.^{18,19} The main obstacles of the CVD method are the harsh synthesis conditions (high temperature

^a School of Science, State Key Laboratory for Mechanical Behavior of Materials, MOE Key Laboratory for Nonequilibrium Synthesis and Modulation of Condensed Matter, Xi'an Jiaotong University, Xi'an 710049, China. E-mail: menglingjie@mail.xjtu.edu.cn

^b Instrumental Analysis Center, Xi'an Jiaotong University, Xi'an 710049, China

† Electronic supplementary information (ESI) available: SEM images and XRD patterns of MoS₂ nanocones and nanoworms; EDS mapping and elemental analyses of WS₂ nanocones, nanoworms, and nanosheets, and MoS₂ nanocones; XPS spectra of WS₂ and MoS₂ nanocones and nanoworms; experimental parameters of the obtained WS₂ nanostructure. See DOI: 10.1039/c8ce00057c

and inert atmosphere) and complicated transfer of TMD sheets from growth substrates.²⁰ Wet-chemical synthesis methods including hydro-/solvochemical syntheses represent good choices for the preparation of 2D nanomaterials with high yields, which are especially useful for applications where bulk quantities with various sizes and thicknesses are desirable.

Among all the TMDs, MoS₂ nanosheets are the easiest to be synthesized by a hydro- or solvochemical route. However, only a small number of research papers report preparation of WS₂ nanosheets. For example, Chhowalla and Shin's group successfully employed WCl₆ and thioacetamide (TAA) to synthesize WS₂ nanosheets by a typical one-pot hydrothermal reaction.²¹ This method has been widely used for various applications,^{22–25} though some impurities including one-dimensional nanostructures and tungsten oxide intermediates were found. As far as we know, WO_x is commonly used in CVD processes, whereas WO_x tends to be chemically reduced to form zero-dimensional or one-dimensional nanostructures rather than layered compounds *via* hydrothermal treatment.^{21,26} It seems that this method can actually be more useful for preparation of 3D WS₂ and graphene oxide composites rather than pure WS₂ nanoflakes.^{27–29} Recently, M. Terrones and R. E. Schaak *et al.* well synthesized WS₂ and TMD alloy nanostructures in CS₂ through a relatively complicated process.³⁰ Huang's group improved the preparation of WS₂ nanosheets by mixing (NH₄)₁₀W₁₂O₄₁·xH₂O and thiourea *via* hydrothermal treatment.³¹ Yet it is still a great challenge to synthesize WS₂ nanosheets with controlled morphologies and with minimum impurities such as tungsten oxides.

WS₂ and other TMD nanostructures have been applied in photothermal therapy.^{32,33} To reduce the side effects and drug resistance of chemotherapy,^{34,35} photothermal therapy is an alternative cancer treatment approach that employs a photo-absorber to convert laser radiation to heat to ablate cancer cells because the tumor cells are more sensitive to heat than healthy cells, and thus, hyperthermia can kill target cells with minimal side effects. Furthermore, a near-infrared (NIR, 808 nm in particular) laser is preferred as it is able to penetrate skin and tissues to a reasonable depth.^{36,37} Developing highly efficient photo-absorbers is one of the key technologies for photothermal therapy.

Herein, we report a facile and effective microwave-assisted solvochemical method for the synthesis of high-quality WS₂ nanomaterials with controllable sizes and morphologies. We used *N*-methyl-2-pyrrolidone (NMP) as the synthesis medium and tungsten hexachloride (WCl₆) and sublimed sulfur (S) as initial reactants. WCl₆ can be well dissolved in NMP, which helps to avoid non-reducible WO_x. This fact is very beneficial for the formation of uniform and high-quality WS₂ nanomaterials. NMP is a polar solvent with a high boiling point. The microwave-assisted strategy is based on special heating mechanisms, dipolar polarization and ionic conduction.³⁸ In addition, NMP provides a reducing environment and is one of the most suitable solvents to disperse TMD nanomaterials. The effects of reactant concentration, reaction time and tem-

perature on the resulting products are investigated in detail. By adjusting the reaction conditions, we are able to synthesize WS₂ nanosheets with different morphologies including hierarchical cone-like and worm-like WS₂. As a new developed photothermal reagent, the photothermal performances of WS₂ with different morphologies were compared. This facile and effective route has also been successfully applied in the preparation of other layered transition-metal materials, such as MoS₂.

Experimental

2.1 Materials

Tungsten hexachloride (WCl₆, 99.0%), molybdenum pentachloride (MoCl₅, 99.6%), *N*-methyl-2-pyrrolidone (NMP, 99.0%) and sublimed sulfur (S, 99.5%) were purchased from Aladdin Industrial Corporation. All reagents were used as received without further purification. Ultrapure water (18.2 MΩ cm) obtained from a Millipore Milli-Q purification system was used throughout the experiments.

2.2 Preparation of layered WS₂ and MoS₂ nanomaterials

A multi-mode microwave parallel synthesis system (XH-800S, China) at a frequency of 2.45 GHz was used to perform the synthesis of WS₂ and MoS₂. In general, certain amounts of WCl₆ and elemental sulfur were dissolved in NMP (30 mL) with simultaneous vigorous stirring for about 30 min to form a homogenous mixture. After that, the resulting mixture was transferred into a 50 mL microwave reaction kettle for the microwave-assisted solvochemical synthesis. Black precipitates formed after 6–8 h. After cooling to room temperature, it was centrifuged and the solid was washed with distilled water (3 × 20 mL) and ethanol (3 × 20 mL). The black powder was then dried under vacuum at 50 °C for 12 h. The resulting WS₂ nanomaterials were then annealed at 850 °C for 1 hour at 2 × 10⁻³ mbar. Details of the reaction conditions including the amount of precursors, the reaction temperature and the time during the solvochemical synthesis for three different morphologies of WS₂ are listed in Table S1.† Layered MoS₂ nanomaterials can be synthesized using the same procedure using MoCl₅.

2.3 Characterization

Transmission electron microscopy (TEM) images were recorded on a TEM-2100 electron microscope at 200 kV (JEOL, Japan), and high-resolution transmission electron microscopy (HR-TEM) was conducted on a TEM-F200 electron microscope at 200 kV (JEOL, Japan). TEM samples were prepared by the deposition of 5 μL dilute solution on a copper grid and subsequent drying at ambient temperature prior to analysis. Scanning electron microscopy (SEM) was performed on a GeminiSEM-500 equipped with an energy dispersive X-ray spectroscope (EDS) at 30 kV (Zeiss, Germany). X-ray diffraction (XRD) patterns were recorded on a D8 ADVANCE X-ray diffractometer using Cu-Kα radiation ($\lambda = 1.5418 \text{ \AA}$) at

an operating voltage of 30 kV and a current of 10 mA (Bruker, Germany). Diffraction patterns were collected from 10° to 80° at a speed of 8° min^{-1} . X-ray photoelectron spectroscopy (XPS) was carried out at room temperature on an ESCALAB Xi⁺ spectrometer (Thermo Fisher Scientific, US) with a double anode Al/Mg target X-ray source (400 W). The C 1s peak at 284.8 eV is the criterion for all binding energies. We have considered the Shirley background in the process of fractal fitting. Raman spectroscopy with irradiation at 532 nm was performed on a YVON HR800 Raman spectroscope (Horiba, Japan, 10 mW) from 200 to 600 cm^{-1} . UV-vis-NIR absorption spectra were obtained using a Lambda35 UV-vis spectrophotometer (PerkinElmer, US).

2.4 Photothermal experiments

The WS₂ nanomaterial suspension was placed in a plastic tube ($10 \times 10 \times 20 \text{ mm}^3$) at a distance of 10 cm from the laser source (808 nm wavelength and spot size 0.75 cm^2) at a power density of 1.5 W cm^{-2} . The temperature curve for the suspension was recorded within 10 min using a digital thermometer (accuracy 0.11° C , OMEGA Engineering Inc.) and OM-CP Data Logger software.

Results and discussion

The WS₂ nanosheets and assemblies were synthesized through a facile, high-throughput and low-cost microwave-assisted solvothermal process (Scheme 1). Compared to the long synthesis time of the traditional hydrothermal method ($>48 \text{ h}$), the microwave-assisted solvothermal reaction is considerably faster (within 8 h), with a high yield ($>90\%$) and satisfactory reproducibility. NMP was selected as the solvent because it can dissolve well both WCl₆ and S and its dipolar polarization and high boiling point make it suitable for the microwave-assisted solvothermal process. In addition, NMP provides a reducing environment to minimize the formation of WO_x. The morphologies of resulting WS₂ were controlled by adjusting the reactant concentration, reaction time and temperature.

Firstly, the effect of reaction temperature on the WS₂ morphology was investigated and it was found that the structure of the resulting WS₂ is sensitive to temperature as indicated by the SEM analysis of the obtained products at varying temperatures (Fig. 1). At the same concentration of WCl₆ and S

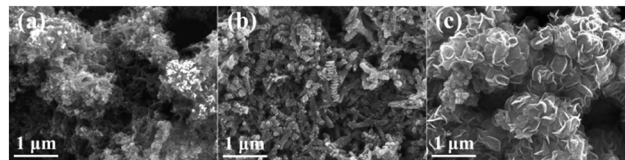
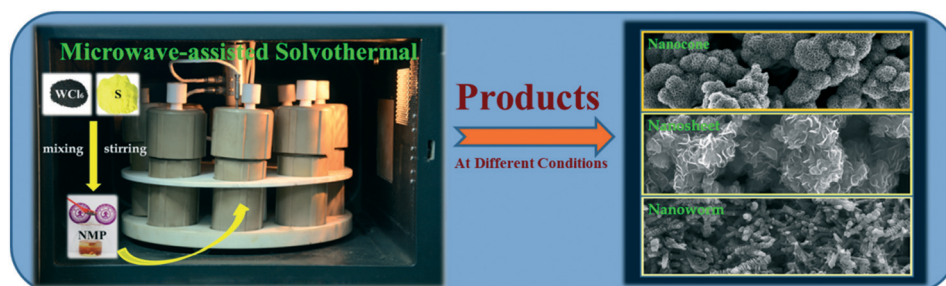


Fig. 1 SEM images of WS₂ by reaction of WCl₆ (0.446 g, 1.125 mmol) and S (0.72 g, 22.5 mmol) for 7 h at (a) 200 °C, (b) 220 °C and (c) 240 °C.

with the same reaction time, WS₂ nanoworms with some irregular nanoparticles were formed at 200 °C (Fig. 1a). When the reaction temperature was increased to 220 °C, uniform and hierarchical WS₂ nanoworms with a bigger diameter were obtained (Fig. 1b). When the reaction temperature was further increased to 240 °C, WS₂ nanosheets with sizes over 300 nm were formed (Fig. 1c). It is clear that the reaction temperature is a key factor in controlling the morphology of WS₂, as the growth of WS₂ is controlled simultaneously by the thermodynamics and the kinetics of the reaction.³⁹ The nucleation rate and crystal growth rate increased with increasing reaction temperature. However, if the crystals grow too rapidly then the formation of larger nanoworms will be less possible, as the alignment of large nanosheets requires longer time.

The effect of WCl₆ and S concentrations on the morphology of WS₂ was also studied at 220 and 240 °C, respectively (Fig. 2). The SEM analysis shows that at 220 °C, WS₂ nanoworms were always obtained when the reaction time and temperature were kept constant. However, when the WCl₆ and S amounts increased from 0.112 g and 0.18 g to 0.446 g and 0.72 g, respectively, the diameter of the nanoworms also increased accordingly (Fig. 2a–c). At 240 °C, three kinds of WS₂ structures (nanoworms, nanosheets and nanocones) were formed at different reactant concentrations (Fig. 2d–f). In all cases, the molar ratio of WCl₆ to S was kept at 1:20 since excessive amounts of S can potentially provide a favorable reducing atmosphere to promote the reaction. We noticed that the high concentration of WCl₆ (0.892 g WCl₆ in 30 mL NMP) resulted in the formation of WS₂ nanocones, and the medium concentration of WCl₆ solution (0.446 g WCl₆ dissolved in 30 mL NMP) benefited the formation of nanosheets. However, the low concentration of WCl₆ (0.112 g WCl₆ in 50 mL NMP) was beneficial for the formation of hierarchical WS₂ nanoworms.



Scheme 1 Schematic illustration of the preparation of WS₂ nanostructures.

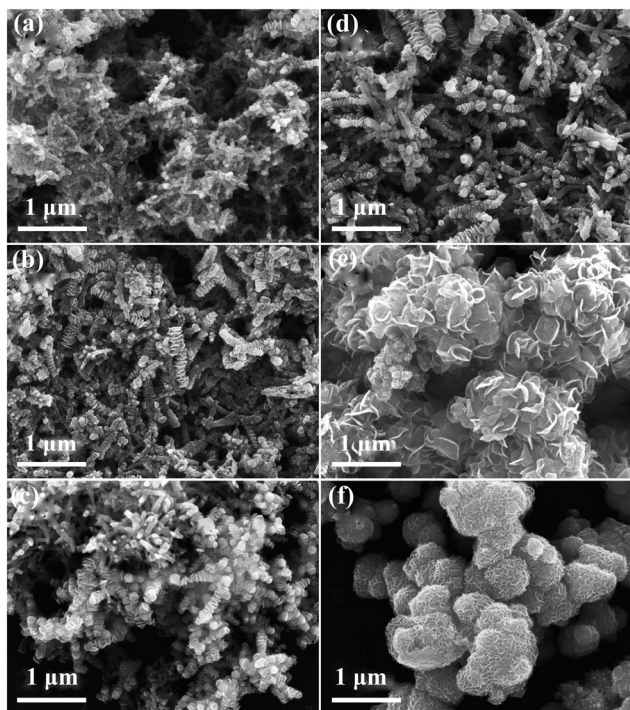


Fig. 2 SEM images of WS_2 obtained at (a–c) 220 °C and (d–f) 240 °C for 7 h. (a and d) WCl_6 (0.112 g, 0.282 mmol), S (0.18 g, 5.625 mmol); (b and e) WCl_6 (0.446 g, 1.125 mmol), S (0.72 g, 22.5 mmol); (c and f) WCl_6 (0.892 g, 2.25 mmol), S (1.44 g, 45 mmol).

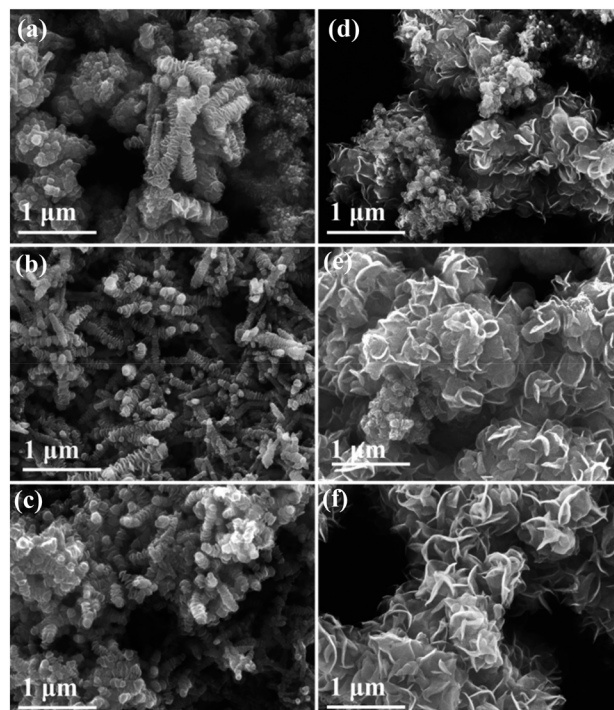


Fig. 3 SEM images of the WS_2 products at 240 °C with reactant concentrations at (a–c) WCl_6 (0.112 g, 0.282 mmol), S (0.18 g, 5.625 mmol); (d–f) WCl_6 (0.446 g, 1.125 mmol), S (0.72 g, 22.5 mmol). (a and d) 6 h; (b and e) 7 h and (c and f) 8 h.

The effect of WCl_6 and S concentrations on the morphology of WS_2 can also be explained by the thermodynamics and kinetics of the reaction. Though the crystal growth rate and nucleation rate are faster at higher reactant concentrations, the nucleation rate is significantly faster than the crystal growth rate at high reactant concentration, which leads to the formation of cone-like aggregates. The crystal growth rate was inversely proportional to the nucleation rate at medium reactant concentration and as a result, loose nanosheets were formed. However, only nanoworms formed at lower reactant concentrations because of the relatively slow nucleation and crystal growth rates.

Previous reports of synthesis of WS_2 nanomaterials required long reaction time.^{21–26} To examine the dependence of the structure of products on the reaction time, we analysed the product structure by freezing the reaction at different intervals with different reactant concentrations. The SEM analysis shows that at 240 °C, WS_2 nanoworms and nanosheets were formed within 6 h (Fig. 3a and d). When the reaction time is extended to 7 h, uniform WS_2 nanoworms and nanosheets are obtained (Fig. 3b and e). By further increasing the reaction time, the morphologies of the WS_2 nanostructures exhibited only negligible change (Fig. 3c and f). Therefore, the optimized reaction time is 7 h for this reaction. Compared to the long synthesis time of the traditional hydrothermal method (>48 h), this microwave-assisted solvothermal reaction is considerably faster, and the obtained products are quite uniform due to the evenly distributed microwave heating.

The morphologies and interlayers of the obtained WS_2 nanoworms, nanosheets and nanocones were analysed in more detail (Fig. 4). The hierarchical worm-like WS_2 nanoparticles consist of WS_2 nanoplates stacked together, each of about 150 nm in size (Fig. 4a and b). The WS_2 nanosheets are composed of loose aggregates of ~300 nm nanosheets (Fig. 4c and d). The interlayer spacing of WS_2 nanosheets, obtained from the HR-TEM images, is measured to be 0.65 nm, which can be attributed to the (002) plane (Fig. 4e), indicating that the WS_2 nanosheets have multi-layer structures. The in-plane lattice spacing is about 0.29 nm (Fig. 4f), which can be attributed to the (101) plane. The cone-like WS_2 are aggregates of small nanoplates (Fig. 4g), and their (101) and (110) diffraction could be clearly observed in the SAED pattern, indicating that WS_2 nanocones have hexagonal phase structures. In fact, this facile microwave-assisted solvothermal method could also be used for preparation of other TMDs such as MoS_2 nanoworms and nanocones (see ESI† Fig. S1).

The crystal structures of the WS_2 nanostructures in Fig. 4 were further examined by X-ray diffraction (XRD) (Fig. 5a). The diffraction peaks were well consistent with the hexagonal phase of WS_2 (JCPDS card no. 87-2417). The peak at ~14.84° was assigned to the (002) planes of WS_2 . The two peaks centered at 33.41° and 58.64° are attributable to the corresponding (101) and (110) planes of layered WS_2 , respectively, which matches well with the results of the SAED pattern in Fig. 4h. The locations and intensities of the diffraction peaks of the

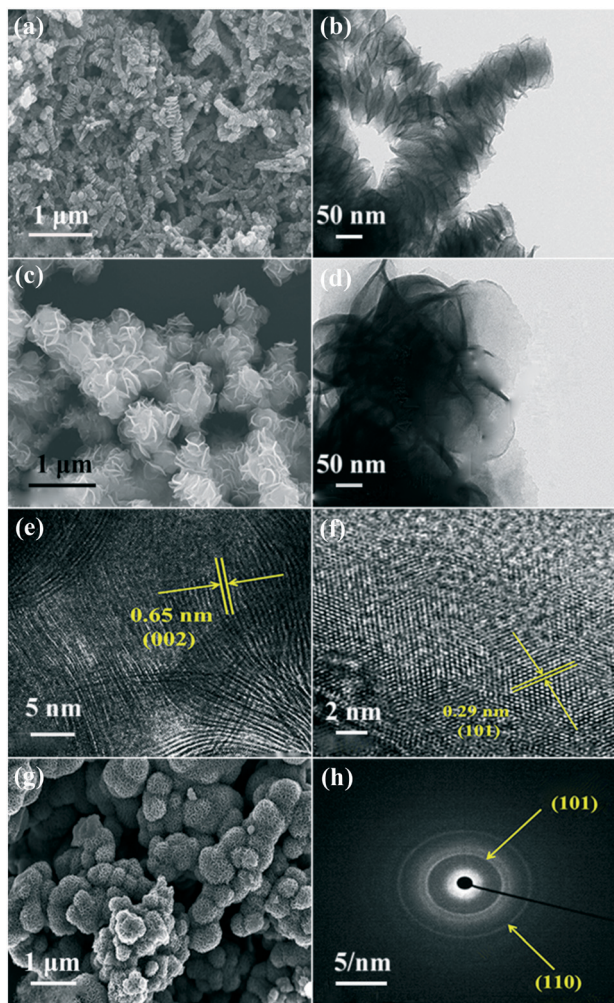


Fig. 4 (a) SEM and (b) TEM images of the WS₂ nanoworms (obtained at 0.112 g, 0.282 mmol WCl₆; 0.18 g, 5.625 mmol S; *T* = 240 °C, *t* = 7 h); (c) SEM, (d) TEM and (e and f) HR-TEM images of WS₂ nanosheets (obtained at 0.446 g, 1.125 mmol WCl₆; 0.72 g, 22.5 mmol S; *T* = 240 °C, *t* = 7 h); (g) SEM image and (h) SAED pattern of WS₂ nanocones (obtained at 0.892 g, 2.25 mmol WCl₆; 1.44 g, 45 mmol S; *T* = 240 °C, *t* = 7 h).

nanocones, nanosheets and nanoworms are somewhat shifted, probably depending on the crystallization of samples. Generally, nanocones have the best crystallinity because their peaks shift to the right with the increase of crystallinity. A special peak marked as #2 in Fig. 5a at 18.27° is probably caused by the remaining impurities including oxides and sulfides. In contrast, the #2 peaks for MoS₂ is negligible (see ESI† Fig. S2) because MoS₂ is not easy to be oxidized during the preparation process and there are a few impurities between interlayers after annealing.⁴⁰ It is noteworthy that the #2 peak of the hierarchical worm-like WS₂ is also very weak probably because only a few impurities can be inserted in the smaller WS₂ petals. It is also possible that this peak is weak because of the formation of monodisperse single-layered WS₂.⁴¹

Raman spectroscopy is carried out to demonstrate the structures and aggregation of WS₂ nanostructures (Fig. 5b).

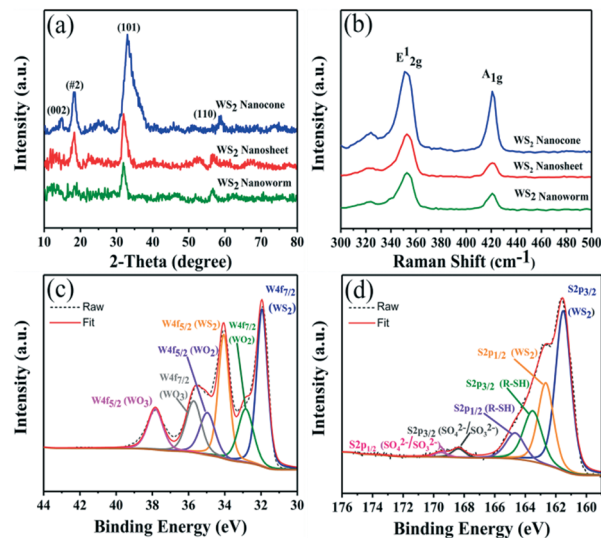


Fig. 5 (a) XRD patterns and (b) Raman spectra of WS₂ nanocones, nanosheets and nanoworms. Elemental XPS spectra of (c) W4f and (d) S2p in WS₂ nanosheets.

Two characteristic peaks of WS₂ at 350 cm⁻¹ and 420 cm⁻¹ correspond to the E_{2g}¹ and A_{1g} modes of layered WS₂, respectively. The intensity of A_{1g} (out-of-plane vibrational mode) was weaker than E_{2g}¹ (in-plane vibrational mode) for the few-layer effect (Fig. 5b). As shown in previous reports, the intensity of the A_{1g} mode was similar to that of the E_{2g}¹ mode for the WS₂ powder.³⁷ The Raman peaks of WS₂ with different morphologies show different intensities probably due to the scattering increase with the density increase.

The elemental composition and distribution of these three WS₂ nanostructures in Fig. 4 were further characterized by energy-dispersive X-ray spectroscopy (EDS) (see ESI† Fig. S3), which clearly shows that the WS₂ nanocones, nanosheets and nanoworms are mainly composed of W and S elements. The corresponding elemental mapping results distinctly indicate that the W and S elements co-exist and are evenly distributed. Similarly, the EDS results of MoS₂ give the same evidence that Mo and S elements are uniformly distributed throughout the nanostructures (ESI† Fig. S4).

X-ray photoelectron spectroscopy (XPS) analyzed the chemical states of W and S in WS₂ nanosheets (Fig. 5), nanocones and nanoworms (ESI† Fig. S5). The binding energies of W4f_{7/2} and W4f_{5/2} in WS₂ are 31.94 and 34.06 eV for WS₂ nanosheets (Fig. 5c), 32.69 and 34.83 eV for WS₂ nanocones (ESI† Fig. S5a), and 32.7 and 34.83 eV for hierarchical WS₂ nanoworms (ESI† Fig. S5c), respectively. The peaks of S2p_{3/2} and S2p_{1/2} in WS₂ correspond to 161.51 and 162.66 eV for WS₂ nanosheets (Fig. 5d), 162.36 and 163.57 eV for WS₂ nanocones (ESI† Fig. S5b), and 162.39 and 163.57 eV for hierarchical WS₂ nanoworms (ESI† Fig. S5d), which agree well with the references.^{42,43} In fact, the oxidation of WCl₆ is also a very important factor because of its instability in air. Therefore, some peaks belonging to the various oxides of tungsten could be observed (Fig. 5c and S5a and c†). It is very difficult

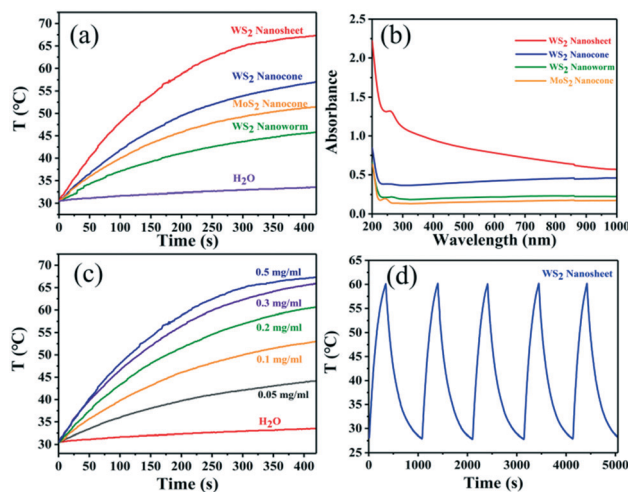


Fig. 6 Photothermal properties of WS₂ structures. (a) Photothermal conversion curves of ultrapure water, WS₂ nanosheet, WS₂ nanocone, WS₂ nanoworm and MoS₂ nanocone aqueous dispersions (0.5 mg mL⁻¹) with time (0–400 s) under 808 nm laser irradiation at a power density of 1.5 W cm⁻². (b) UV-vis-NIR absorption spectra of WS₂ nanosheet, WS₂ nanocone, WS₂ nanoworm and MoS₂ nanocone aqueous dispersions (0.2 mg mL⁻¹). (c) Photothermal conversion curves of WS₂ nanosheets at different concentrations (0.05, 0.1, 0.2, 0.3 and 0.5 mg mL⁻¹) by 808 nm laser irradiation (1.5 W cm⁻²). (d) Temperature variations of WS₂ nanosheets at the concentration of 0.5 mg mL⁻¹ during 5 cycles of intermittent periodic irradiation by an 808 nm laser (1.5 W cm⁻²).

to completely avoid the formation of WO_x during the preparation of WS₂.⁴⁴ However, the WO_x content in our products is much lower than those reported in the literature.³¹ In contrast, negligible MoO_x amounts were found in both MoS₂ nanocones and nanoworms (ESI,† Fig. S6), because Mo is relatively difficult to oxidize.

2D-TMDs including WS₂ have exhibited great potential in many fields including phototherapy agents.^{2,14,45} Here, we compared the photothermal conversion capability of the resulting WS₂ nanocones, WS₂ nanosheets, WS₂ nanoworms and MoS₂ nanocones (Fig. 6a). No significant temperature change was observed when pure water was exposed to 808 nm laser irradiation because water has almost no absorption at 808 nm. Interestingly, when the WS₂ nanosheet aqueous solution (0.5 mg mL⁻¹) was irradiated with the 808 nm laser (1.5 W cm⁻²), the temperature increased rapidly and reached 67 °C within 7 min. Upon irradiation of aqueous solutions of WS₂ nanocones and nanoworms, the temperature also increases but to a much less extent. In contrast, WS₂ nanosheets have the best photothermal conversion capability probably because WS₂ nanosheets have the biggest specific surface area and tend to absorb more photons at the same concentration.

Besides, naturally, WS₂ nanocones have much better photothermal conversion capability than MoS₂ nanocones. The UV-vis-NIR absorption experiments provide further evidence that the absorption of TMDs at 808 nm is closely related to their morphologies and the WS₂ nanosheets have the biggest absorption in the NIR region (Fig. 6b). In addition, the temperature rising rate is positively correlated with the concentration of WS₂ nanosheets (Fig. 6c): the higher the

concentration of WS₂ nanosheet aqueous solution, the higher the temperature increase within 7 min. This concentration dependence is not unexpected as the nanosheets can harvest NIR photons more effectively at higher concentrations and convert them to heat. In fact, low concentration of WS₂ nanosheets (*i.e.* 0.05 or 0.1 mg mL⁻¹) seems to be enough for photothermal therapy because most of the tumor cells can be killed at 42–43 °C.^{14,46}

The photothermal stability of the WS₂ nanosheets was also determined since an effective photothermal material should be stable during the process of irradiation. WS₂ nanosheets (0.5 mg mL⁻¹) displayed satisfactory photothermal stability during 5 cycles of intermittent irradiation by the 808 nm laser (1.5 W cm⁻²) (Fig. 6d). Overall, WS₂ nanosheets have great potential for photothermal conversion due to their excellent conversion efficiency and thermal stability.

Conclusions

In conclusion, we developed a simple and efficient microwave-assisted solvothermal method to synthesize WS₂ nanostructures in NMP by using inexpensive tungsten hexachloride (WCl₆) and sulfur (S) as initial reactants. The morphology and structures of WS₂ including nanocones, nanosheets and nanoworms could be well-controlled by adjusting the reactant concentration and reaction temperature. This method could be also successfully applied for preparation of other transition-metal dichalcogenides such as MoS₂. Among the WS₂ and MoS₂ nanomaterials, WS₂ nanosheets have the best photothermal effect and exhibit a very stable photothermal capacity even after five cycles. Thus, they show potential to be widely used for photothermal therapy and other fields.

Conflicts of interest

The authors declare no competing financial interest.

Acknowledgements

This work was supported by the National Natural Science Foundation of China (21474079, 21674085), and the Program for New Century Excellent Talents in University (NCET-13-0453). We thank the International Center for Dielectric Research (ICDR) and Instrumental Analysis Center (IAC) of Xi'an Jiaotong University for their support in XPS, SEM, TEM and Raman analyses.

Notes and references

- S. Z. Butler, S. M. Hollen, L. Y. Cao, Y. Cui, J. A. Gupta, H. R. Gutierrez, T. F. Heinz, S. S. Hong, J. X. Huang, A. F. Ismach, E. Johnston-Halperin, M. Kuno, V. V. Plashnitsa, R. D. Robinson, R. S. Ruoff, S. Salahuddin, J. Shan, L. Shi, M. G. Spencer, M. Terrones, W. Windl and J. E. Goldberger, *ACS Nano*, 2013, 7, 2898–2926.
- C. Tan and H. Zhang, *Chem. Soc. Rev.*, 2015, 44, 2713–2731.

- 3 Q. H. Wang, K.-Z. Kourosch, A. Kis, J. N. Coleman and M. S. Strano, *Nat. Nanotechnol.*, 2012, 7, 699–712.
- 4 M. Chhowalla, H. S. Shin, G. Eda, L. J. Li, K. P. Loh and H. Zhang, *Nat. Chem.*, 2013, 5, 263–275.
- 5 Y. Liu, W. Wang, H. Huang, L. Gu, Y. Wang and X. Peng, *Chem. Commun.*, 2014, 50, 4485–4488.
- 6 L. Zhang, W. Fan and T. Liu, *Nanoscale*, 2016, 8, 16387–16394.
- 7 N. Huo, J. Kang, Z. Wei, S.-S. Li, J. Li and S.-H. Wei, *Adv. Funct. Mater.*, 2014, 24, 7025–7031.
- 8 C. R. Wu, X. R. Chang, T. W. Chu, H. A. Chen, C. H. Wu and S. Y. Lin, *Nano Lett.*, 2016, 16, 7093–7097.
- 9 B. Seo, H. Y. Jeong, S. Y. Hong, A. Zak and S. H. Joo, *Chem. Commun.*, 2015, 51, 8334–8337.
- 10 D. Voiry, M. Salehi, R. Silva, T. Fujita, M. Chen, T. Asefa, V. B. Shenoy, G. Eda and M. Chhowalla, *Nano Lett.*, 2013, 13, 6222–6227.
- 11 X. Zhao, X. Ma, J. Sun, D. Li and X. Yang, *ACS Nano*, 2016, 10, 2159–2166.
- 12 L. Cheng, J. Liu, X. Gu, H. Gong, X. Shi, T. Liu, C. Wang, X. Wang, G. Liu, H. Xing, W. Bu, B. Sun and Z. Liu, *Adv. Mater.*, 2014, 26, 1886–1893.
- 13 X. Li, J. Shan, W. Zhang, S. Su, L. Yuwen and L. Wang, *Small*, 2017, 13, 1602660.
- 14 Y. Chen, C. Tan, H. Zhang and L. Wang, *Chem. Soc. Rev.*, 2015, 44, 2681–2701.
- 15 J. N. Coleman, M. Lotya, A. O'Neill, S. D. Bergin, P. J. King, U. Khan, K. Young, A. Gaucher, S. De, R. J. Smith, I. V. Shvets, S. K. Arora, G. Stanton, H.-Y. Kim, K. Lee, G. S. Duesberg, G. T. Kim, T. Hallam, J. J. Boland, J. J. Wang, J. C. Grunlan, J. F. Donegan, G. Moriarty, A. Shmeliov, R. J. Nicholls, J. M. Perkins, E. M. Grievson, K. Theuwissen, D. W. McComb, P. D. Nellist and V. Nicolosi, *Science*, 2017, 331, 568–571.
- 16 H. Feng, Z. Hu and X. Liu, *Chem. Commun.*, 2015, 51, 10961–10964.
- 17 G. Zhao, Y. Wu, Y. Shao and X. Hao, *Nanoscale*, 2016, 8, 5407–5411.
- 18 M. Okada, T. Sawazaki, K. Watanabe, T. Taniguchi, H. Hibino, H. Shinohara and R. Kitaura, *ACS Nano*, 2014, 8, 8273–8277.
- 19 J.-G. Song, J. Park, W. Lee, T. Choi, H. Jung, C. W. Lee, S.-H. Hwang, J. M. Myoung, J.-H. Jung, S.-H. Kim, C. Lansalot-Matras and H. Kim, *ACS Nano*, 2013, 7(12), 11333–11340.
- 20 S. J. Xu, Z. Y. Lei and P. Y. Wu, *J. Mater. Chem. A*, 2015, 3, 16337–16347.
- 21 J. Yang, D. Voiry, S. J. Ahn, D. Kang, A. Y. Kim, M. Chhowalla and H. S. Shin, *Angew. Chem., Int. Ed.*, 2013, 52, 13751–13754.
- 22 L. Zhou, S. Yan, Z. Lin and Y. Shi, *Mater. Chem. Phys.*, 2016, 171, 16–21.
- 23 Q. He, W. Xu, S. Chen, D. Liu, M. Habib, Q. Liu, C. Wang, Y. A. Haleem, T. Xiang, C. Wu, A. Khalil, Q. Fang, Z. Niu and L. Song, *RSC Adv.*, 2016, 6, 87919–87925.
- 24 N. T. Shelke and B. R. Karche, *J. Alloys Compd.*, 2015, 653, 298–303.
- 25 J. Zhang, Q. Wang, L. Wang, X. Li and W. Huang, *Nanoscale*, 2015, 7, 10391–10397.
- 26 H. S. S. R. Matte, A. Gomathi, A. K. Manna, D. J. Late, R. Datta, S. K. Pati and C. N. R. Rao, *Angew. Chem.*, 2010, 122, 4153–4156.
- 27 Q. Liu, C. Sun, Q. He, A. Khalil, T. Xiang, D. Liu, Y. Zhou, J. Wang and L. Song, *Nano Res.*, 2015, 8, 3982–3991.
- 28 G. Huang, H. Liu, S. Wang, X. Yang, B. Liu, H. Chen and M. Xu, *J. Mater. Chem. A*, 2015, 3, 24128–24138.
- 29 S. Cao, T. Liu, W. Zeng, S. Hussain, X. Peng and F. Pan, *J. Mater. Sci.: Mater. Electron.*, 2014, 25, 4300–4305.
- 30 Y. Sun, K. Fujisawa, Z. Lin, Y. Lei, J. S. Mondschein, M. Terrones and R. E. Schaak, *J. Am. Chem. Soc.*, 2017, 139, 11096–11105.
- 31 K. Yang, X. Wang, H. Li, B. Chen, X. Zhang, S. Li, N. Wang, H. Zhang, X. Huang and W. Huang, *Nanoscale*, 2017, 9, 5102–5109.
- 32 Z. B. Li and S. L. Wong, *Mater. Sci. Eng., C*, 2017, 70, 1095–1106.
- 33 C. Z. Zhu, D. Du and Y. H. Lin, *Biosens. Bioelectron.*, 2017, 89, 43–55.
- 34 R. L. Siegel, K. D. Miller and A. Jemal, *Ca-Cancer J. Clin.*, 2016, 66, 7–30.
- 35 T. M. Allen and P. R. Cullis, *Adv. Drug Delivery Rev.*, 2013, 65, 36–48.
- 36 P. T. Wong and S. K. Choi, *Chem. Rev.*, 2015, 115, 3388–3432.
- 37 S. Wang, X. Li, Y. Chen, X. Cai, H. Yao, W. Gao, Y. Zheng, Y. X. An, J. Shi and H. Chen, *Adv. Mater.*, 2015, 27, 2775.
- 38 N. Liu, Y. Guo, X. Yang, H. Lin, L. Yang, Z. Shi, Z. Zhong, S. Wang, Y. Tang and Q. Gao, *ACS Appl. Mater. Interfaces*, 2015, 7, 23741–23749.
- 39 H.-Y. Wang, B.-Y. Wang, D. Wang, L. Lu, J.-G. Wang and Q.-C. Jiang, *RSC Adv.*, 2015, 5, 58084–58090.
- 40 H. Jiang, D. Ren, H. Wang, Y. Hu, S. Guo, H. Yuan, P. Hu, L. Zhang and C. Li, *Adv. Mater.*, 2015, 27, 3687–3695.
- 41 M. Zhou, Z. Zhang, K. Huang, Z. Shi, R. Xie and W. Yang, *Nanoscale*, 2016, 8, 15262–15272.
- 42 S. Yu, J. W. Jung and I. D. Kim, *Nanoscale*, 2015, 7, 11945–11950.
- 43 W. Yang, J. Wang, C. Si, Z. Peng, J. Frenzel, G. Eggeler and Z. Zhang, *J. Mater. Chem. A*, 2015, 3, 17811–17819.
- 44 T. Lei, W. Chen, J. Huang, C. Yan, H. Sun, C. Wang, W. Zhang, Y. Li and J. Xiong, *Adv. Energy Mater.*, 2017, 7, 1601843.
- 45 S. Wang, J. Zhao, H. Yang, C. Wu, F. Hu, H. Chang, G. Li, D. Ma, D. Zou and M. Huang, *Acta Biomater.*, 2017, 58, 442–454.
- 46 G. Yang, H. Gong, T. Liu, X. Sun, L. Cheng and Z. Liu, *Biomaterials*, 2015, 60, 62–71.